



A Hybrid Finite-Difference-Particle Method for Chemotaxis Models

Alina Chertock¹ · Shumo Cui² · Alexander Kurganov³ · Chenxi Wang²

Received: 5 April 2024 / Revised: 28 March 2025 / Accepted: 4 June 2025

© The Author(s), under exclusive licence to Springer Science+Business Media, LLC, part of Springer Nature 2025

Abstract

Chemotaxis systems play a crucial role in modeling the dynamics of bacterial and cellular behaviors, including propagation, aggregation, and pattern formation, all under the influence of chemical signals. One notable characteristic of these systems is their ability to simulate concentration phenomena, where cell density undergoes rapid growth near specific concentration points or along certain curves. Such growth can result in singular, spiky structures and lead to finite-time blowups. Our investigation focuses on the dynamics of the Patlak-Keller-Segel chemotaxis system and its two-species extensions. In the latter case, different species may exhibit distinct chemotactic sensitivities, giving rise to very different rates of cell density growth. Such a situation is highly challenging for numerical methods as they may fail to accurately capture the blowup of the slower-growing species mainly due to excessive numerical dissipation. In this paper, we propose a hybrid finite-difference-particle (FDP) method, in which a sticky particle method is used to solve the chemotaxis equation(s), while finite difference schemes are employed to solve the chemoattractant equation. Thanks to the low-dissipation nature of the sticky particle method, the proposed hybrid scheme is particularly adept at capturing the blowup behaviors in both one- and two-species cases. The proposed hybrid FDP methods are tested on a series of challenging examples, and the obtained numerical results demonstrate that our hybrid method can provide sharp resolution of the singular structures even with a relatively small number of particles. Moreover, in the case of the two species, our method adeptly captures the blowing-up solution for the component with lower chemotactic sensitivity, a feature not observed in other works.

✉ Chenxi Wang
wangcx2017@mail.sustech.edu.cn

Alina Chertock
chertock@math.ncsu.edu

Shumo Cui
cuism@sustech.edu.cn

Alexander Kurganov
alexander@sustech.edu.cn

¹ Department of Mathematics, North Carolina State University, Raleigh, NC 27695, USA

² Shenzhen International Center for Mathematics, Southern University of Science and Technology (SUSTech), Shenzhen 518055, People's Republic of China

³ Department of Mathematics and Shenzhen International Center for Mathematics, Southern University of Science and Technology (SUSTech), Shenzhen 518055, People's Republic of China

Keywords Patlak-Keller-Segel chemotaxis systems · Two-species chemotaxis · Sticky particle method · Finite-difference schemes · Blow up

AMS subject classification 65M75 · 65M06 · 76M28 · 92C17 · 35M10

1 Introduction

We consider the two-dimensional (2-D) two-species Patlak-Keller-Segel (PKS) type chemotaxis system:

$$\begin{cases} (\rho_1)_t + \chi_1 \nabla \cdot (\rho_1 \nabla c) = \nu_1 \Delta \rho_1, & (1.1a) \\ (\rho_2)_t + \chi_2 \nabla \cdot (\rho_2 \nabla c) = \nu_2 \Delta \rho_2, & (1.1b) \\ \tau c_t = \nu \Delta c + \gamma_1 \rho_1 + \gamma_2 \rho_2 - \zeta c, & (1.1c) \end{cases}$$

where $\mathbf{x} = (x, y)^\top \in \Omega \subset \mathbb{R}^2$ are the spatial variables, t is time, ρ_1 and ρ_2 represent the cell densities of two non-competing species, c is the concentration of the chemoattractant, $\chi_2 > \chi_1 > 0$ are the chemotactic sensitivity parameters, ν_1, ν_2 , and ν are the diffusion coefficients, γ_1 and γ_2 represent chemoattractant production rates, and ζ represents chemoattractant decay rate ($\nu_1, \nu_2, \nu, \gamma_1, \gamma_2$, and ζ are positive constants). The parameter τ is either 0 or 1, corresponding to the case of parabolic-elliptic or parabolic-parabolic coupling, respectively. The system (1.1) is considered subject to certain initial data and the homogeneous Neumann boundary conditions.

The original single-species PKS chemotaxis model, which can be obtained from the system (1.1) by setting $\rho_2 \equiv 0$, was first introduced in [35, 36, 40] and later extended to the two-species system (1.1) in [46]. Analytical investigations followed in [20, 26, 27, 32–34, 39, 44]. Depending on the initial data, boundary conditions, and parameter values, the solution may either converge to a constant steady state or develop singular structures (blow up in finite time). In blowup scenarios, different blowup time scales are anticipated for the two densities, with ρ_2 possibly blowing up faster than ρ_1 . However, as proved in [26, 27], simultaneous blowup is the only possibility in the parabolic-elliptic case ($\tau = 0$), even though different scalings may exist for the two species. This poses a significant challenge in developing accurate and robust numerical methods for (1.1).

To the best of our knowledge, the first numerical method for (1.1) was introduced in [37], where the system (1.1) was solved by a second-order hybrid finite-volume-finite-difference method proposed in [10] for the single-species PKS system. It was observed in [37] that when $\chi_2 \gg \chi_1$, the cell densities ρ_1 and ρ_2 exhibit different blowup behaviors: ρ_2 develops a δ -type singularity, whereas ρ_1 undergoes algebraic blowup. This observation was numerically validated by conducting a very careful mesh refinement study. However, the obtained results were misleading since only algebraic growth—not blowup—of ρ_1 could be observed due to inadequate resolution (even on a very fine mesh). A fourth-order hybrid finite-volume-finite-difference method developed in [10] helped only slightly to enhance the resolution. More recently, in [15], an adaptive moving mesh (AMM) finite-volume semi-discrete upwind method was introduced to enhance the approximation of singular structures of ρ_1 in the two-species chemotaxis system. Despite this advancement, the numerical experiments reported in [15] show that even the AMM method failed to accurately capture the ρ_1 -component of the blowing-up solution when $\chi_2 \gg \chi_1$.

In this paper, we introduce a hybrid finite-difference-particle (FDP) approach for capturing the singular behavior of solutions of (1.1). In order to achieve a high resolution of both components of the blowing up solution (ρ_1 and ρ_2), we employ a sticky particle method introduced in [5, 16] in the context of pressureless gas dynamics equations, to the chemotaxis equations (1.1a) and (1.1b), while applying a second-order finite-difference (FD) semi-discrete scheme for solving the chemoattractant equation (1.1c).

Sticky particle methods belong to a class of deterministic particle methods, which provide a diffusion-free (or low diffusion) alternative to Eulerian methods for a variety of time-dependent PDEs; see, e.g., [6, 16] and references therein. In these methods, the numerical solution is sought as a linear combination of Dirac distributions (δ -functions), whose positions and coefficients represent the locations and weights of the particles, respectively. The solution is then found by following the time evolution of the locations and weights of the particles according to a system of ODEs obtained by considering a weak formulation of the studied PDEs. Even though over the years deterministic particle methods were mainly used to numerically solve purely convective equations (see, e.g., [21, 42, 43] and references therein), the range of applicability of these methods was extended to treat convection-diffusion and other types of equations (see, e.g., [4, 8, 17, 21–25, 38, 42]). Several approaches have been explored for treating diffusion terms in particle methods. One of the widely used treatments is the random walk approach [19, 30], in which the diffusion operator is naturally approximated by adding a Wiener process to the motion of each particle. This way, the diffusion only affects the positions of particles—not their weights. A drawback of the random walk method, like other stochastic methods, is that its accuracy is very low, and reasonable resolutions can be achieved only if a very large number of realizations is used, which would make the particle method for the PKS-type systems extremely inefficient. Among the deterministic approaches, the one we have successfully implemented in this paper is a weighted particles method [23, 24, 38], which is both efficient and accurate. In this method, the diffusion is first approximated by an integral operator, which is then treated as a source term that affects the particle weights—not their positions.

As mesh-free, particle methods are quite flexible as the particle positions are self-adapted to the local flow. This, however, comes at the expense of the regularity of the particle distribution: inter-particle distances typically change in time, and just as particles may cluster, they may also spread away from each other. This may lead to a poor resolution of the computed solution and a low efficiency of the particle method. The latter is related to the fact that the time-step for the ODE solver used to evolve the particle system in time depends generally on the distance between the neighboring particles. Thus, the success of deterministic particle methods relies upon an accurate and efficient particle redistribution algorithm, which ensures that different parts of the computed solution are adequately resolved. A large variety of re-meshing techniques has been proposed (see, e.g., [6, 9, 11, 13, 17, 18, 22, 25, 41] to name a few), including the particle merger approach used in [13, 18, 22]. Particle merger becomes crucial in cases when the solution naturally develops sharp spikes or even δ -type singularities. In these cases, the clustering particles must be merged into heavier particles located in the center of mass of the merged particles: this is the key feature of the sticky particle methods, which were successfully applied to the pressureless gas dynamics equations [16] and dusty gas flows [7].

The success of the proposed hybrid FDP method hinges on the accurate and efficient computations of the values of c at the particle locations and the projection of the particle approximations onto the nodes of the FD grid. The former is achieved with the help of a global piecewise linear approximation of c (this technique is borrowed from the finite-

volume methods; also see the finite-volume-particles methods in [7, 16]), while for the latter one, we introduce a new particle-grid projection approach.

The paper is organized as follows. In §2, we give a brief overview of the weighted particle method for convection-diffusion equations. In §3, we introduce a hybrid FDP method, whose components—a novel sticky particle method for the cell densities equations and a second-order FD scheme for the chemoattractant equations—are described in §3.1 and §3.2, respectively. Details of the projection between the particle and grid data, which needs to be performed in the hybridization algorithm, are discussed in §3.3. The numerical algorithm is summarized in §3.4. In §4, we demonstrate the performance of the hybrid FDP method on a number of challenging numerical examples designed to demonstrate the capability of the proposed method to resolve the blowup solution behavior with high resolution. Finally, we conclude the paper in §5 by summarizing our contributions.

2 Weighted Particle Method: an Overview

In this section, we briefly describe the weighted particle method for 2-D convection-diffusion equations. We consider the following model problem:

$$\rho_t + \nabla \cdot (\rho \mathbf{u}) = v \Delta \rho, \quad \mathbf{x} \in \Omega \subset \mathbb{R}^2, \quad t > 0, \quad (2.1)$$

subject to the initial data

$$\rho(\mathbf{x}, 0) = \rho_0(\mathbf{x}). \quad (2.2)$$

Here, $\rho(\mathbf{x}, t)$ is an unknown function, $\mathbf{u}(\mathbf{x}, t) = (u(\mathbf{x}, t), v(\mathbf{x}, t))^T$ is the given velocity field, v is a positive diffusion coefficient, and $\rho_0(\mathbf{x})$ is a given function. Notice that equations (1.1a) and (1.1b) would read as the convection-diffusion equation (2.1) if one replaces ∇c there with a given velocity field. Dependence of (1.1a) and (1.1b) on the chemoattractant equation (1.1c) makes the development of particle methods for (1.1a) and (1.1b) substantially more challenging, as discussed in §3.1, where we develop a new sticky particle method for chemotaxis equations.

In order to apply a weighted particle method to (2.1), one first needs to replace the Laplacian operator $\Delta \rho$ on the right-hand side of (2.1) with its integral approximation to obtain (see, e.g., [6, 23, 24, 38]),

$$\rho_t^\sigma(\mathbf{x}, t) + \nabla \cdot (\rho^\sigma(\mathbf{x}, t) \mathbf{u}(\mathbf{x}, t)) = \frac{v}{\sigma^2} \iint_{\mathbb{R}^2} \eta_\sigma(\mathbf{x} - \mathbf{y}) (\rho^\sigma(\mathbf{y}, t) - \rho^\sigma(\mathbf{x}, t)) \, d\mathbf{y}, \quad (2.3)$$

where σ is a small positive number and

$$\eta_\sigma(\mathbf{x}) := \frac{1}{\sigma^2} \eta\left(\frac{\mathbf{x}}{\sigma}\right), \quad \eta(\mathbf{x}) = \frac{4}{\pi} e^{-|\mathbf{x}|^2}. \quad (2.4)$$

According to [23, Theorem 1], the solution ρ^σ of (2.3) is an approximation of the solution ρ of (2.1) provided \mathbf{u} is sufficiently smooth. We, therefore, aim to find a particle approximation of ρ^σ rather than ρ .

To this end, we seek an approximate solution of (2.3)–(2.4) as a linear combination of Dirac δ -functions,

$$\widehat{\rho}(\mathbf{x}, t) = \sum_{i=1}^N w_i(t) \delta(\mathbf{x} - \mathbf{x}_i(t)), \quad (2.5)$$

where $\mathbf{x}_i(t)$ represents the location of the i -th particle, $w_i(t)$ denotes its weight, and N is the total number of particles. We would like to emphasize that this concept of particles represents a mathematical abstraction, differing from the physical concept of particles of specific materials.

We begin by initializing the particle approximation (2.5). To this end, we divide Ω into a set of non-overlapping subdomains $\{\Omega_i(0)\}_{i=1}^N$:

$$\Omega = \bigcup_{i=1}^N \Omega_i(0) \quad \text{and} \quad \Omega_i(0) \cap \Omega_j(0) = \emptyset \quad \forall i \neq j.$$

We set the initial location of the i -th particle, $\mathbf{x}_i(0)$, to be the center of mass of $\Omega_i(0)$. The corresponding initial weight is then given by $\int_{\Omega_i(0)} \rho(\mathbf{x}, 0) \, d\mathbf{x}$, which we approximate using the midpoint rule resulting in

$$w_i(0) = \rho(\mathbf{x}_i(0), 0) |\Omega_i(0)|. \tag{2.6}$$

We then substitute (2.5) into a weak form of (2.3)–(2.4) to end up with the following system of ODEs for the particle locations $\mathbf{x}_i(t)$, weights $w_i(t)$, and subdomain sizes $|\Omega_i(t)|$:

$$\begin{cases} \frac{d}{dt} \mathbf{x}_i(t) = \mathbf{u}(\mathbf{x}_i(t), t) =: \mathbf{u}_i(t) = (u_i(t), v_i(t))^\top, \\ \frac{d}{dt} w_i(t) = \frac{\nu}{\sigma^2} \sum_{j=1}^N \eta_\sigma(\mathbf{x}_i(t) - \mathbf{x}_j(t)) [w_j(t) |\Omega_i(t)| - w_i(t) |\Omega_j(t)|] =: \beta_i(t), \\ \frac{d}{dt} |\Omega_i(t)| = \nabla \cdot \mathbf{u}(\mathbf{x}_i(t), t) |\Omega_i(t)| = \nabla \cdot \mathbf{u}_i(t) |\Omega_i(t)|. \end{cases} \tag{2.7}$$

The initial conditions for this ODE system are specified in (2.6).

The ODE system (2.7) is to be numerically integrated by an appropriate ODE solver with a time-step Δt , which is chosen to satisfy several requirements. Specifically, the time-step should depend on the distance between nearby particles as the stability condition imposes that no particle trajectories should intersect within the time interval $[t, t + \Delta t]$. In addition, one needs to ensure that the weights w_i remain nonnegative for all i (this is extremely important when ρ must remain nonnegative as in the studied case of chemotaxis systems), the size of subdomains Ω_i does not decay too fast, and no particles propagate too far in one time-step.

To quantify the aforementioned requirements, let us assume, for the sake of simplicity, that the system (2.7) is numerically solved by the first-order forward Euler method:

$$\begin{cases} x_i(t + \Delta t) = x_i(t) + \Delta t u_i(t), \\ y_i(t + \Delta t) = y_i(t) + \Delta t v_i(t), \\ w_i(t + \Delta t) = w_i(t) + \Delta t \beta_i(t), \\ |\Omega_i(t + \Delta t)| = |\Omega_i(t)| [1 + \Delta t \nabla \cdot \mathbf{u}_i(t)]. \end{cases} \tag{2.8}$$

In this case, the first two equations in (2.8) imply that the particle trajectories are straight lines on the interval $[t, t + \Delta t]$ and can be described by the following parametric form with parameters τ_i and τ_j for some particles i and j :

$$\begin{cases} x = x_i(t) + \tau_i u_i(t), \\ y = y_i(t) + \tau_i v_i(t), \end{cases} \quad \text{and} \quad \begin{cases} x = x_j(t) + \tau_j u_j(t), \\ y = y_j(t) + \tau_j v_j(t). \end{cases}$$

It is easy to verify that these two straight lines intersect at the point that corresponds to

$$\begin{aligned} \tau_i &= \frac{v_i(t)(x_j(t) - x_i(t)) - u_i(t)(y_j(t) - y_i(t))}{u_i(t)v_j(t) - u_j(t)v_i(t)}, \\ \tau_j &= \frac{v_j(t)(x_j(t) - x_i(t)) - u_j(t)(y_j(t) - y_i(t))}{u_i(t)v_j(t) - u_j(t)v_i(t)}, \end{aligned} \tag{2.9}$$

unless the denominator $u_i(t)v_j(t) - u_j(t)v_i(t)$ vanishes, in which case these two lines are parallel. Notice that the i -th particle will arrive in this intersection point at time $t + \tau_i$ provided $\tau_i > 0$, while the j -th particle will be there at time $t + \tau_j$ provided $\tau_j > 0$. This leads to the following time-step constraint:

$$\Delta t \leq \begin{cases} \min_{(i,j):\tau_i>0,\tau_j>0} \{ \max(\tau_i, \tau_j) \} & \text{if } \exists (i, j) : \tau_i > 0, \tau_j > 0, \\ \infty & \text{otherwise.} \end{cases} \tag{2.10}$$

Remark 2.1 In practice, in order to prevent division by very small numbers, one has to use the formulae in (2.9) only when $|u_i(t)v_j(t) - u_j(t)v_i(t)| > \mu$, where μ is a small positive number.

Next, it follows from the third equation in (2.8) that the weights w_i will remain nonnegative for all i if

$$\Delta t \leq \begin{cases} \min_{i:\beta_i(t)<0} \left\{ -\frac{w_i(t)}{\beta_i(t)} \right\} & \text{if } \min_i \beta_i(t) < 0, \\ \infty & \text{otherwise.} \end{cases} \tag{2.11}$$

Also, from the last equation in (2.8), we conclude that the size of subdomains Ω_i will not decay too fast for a sufficiently small Δt . For instance, one may restrict their decay within one time-step by a factor of 2 by requiring that the RHS of this equation is greater than $\frac{1}{2}|\Omega(t)|$, which leads to the following time-step restriction:

$$\Delta t \leq \begin{cases} \min_{i:\nabla \cdot \mathbf{u}_i(t)<0} \left\{ -\frac{1}{2\nabla \cdot \mathbf{u}_i(t)} \right\} & \text{if } \min_i \nabla \cdot \mathbf{u}_i(t) < 0, \\ \infty & \text{otherwise.} \end{cases} \tag{2.12}$$

Finally, to limit the distance particles can propagate within one time-step, one may require

$$\Delta t \leq \frac{\sqrt{\min_i |\Omega_i(0)|}}{\max_i (\max\{|u_i|, |v_i|\})}. \tag{2.13}$$

Remark 2.2 The time restrictions (2.10)–(2.13) are still valid if a high-order strong stability preserving (SSP) Runge-Kutta or multistep explicit method [28, 29] is used instead of the forward Euler method for time integration, since the SSP methods can be expressed as convex combinations of forward Euler steps.

3 Hybrid FDP Method for (1.1)

We now turn our attention to the PKS-type system (1.1) and introduce an FDP method for its numerical solution. Specifically, the chemotaxis equations (1.1a) and (1.1b) are discretized

using a sticky particle method (§3.1), while the chemoattractant concentration equation (1.1c) is approximated using an FD scheme (§3.2). The coupling between the two ingredients of the FDP methods is carried out using the projection techniques (§3.3).

3.1 Sticky Particle Method for Equations (1.1a) and (1.1b)

Recall that the chemotaxis equations (1.1a) and (1.1b) take the form of the convection-diffusion equation (2.1) with ρ being either ρ_1 or ρ_2 , $v = v_1$ or $v = v_2$, and $\mathbf{u} = \chi_1 \nabla c$ or $\mathbf{u} = \chi_2 \nabla c$, and consequently can be replaced using an integral approximation of the Laplace operator as follows:

$$\left\{ \begin{aligned} (\rho_1^\sigma)_t(x, t) + \chi_1 \nabla \cdot (\rho_1^\sigma(x, t) \nabla c(x, t)) &= \frac{v_1}{\sigma^2} \iint_{\mathbb{R}^2} \eta_\sigma(x - y) (\rho_1^\sigma(y, t) - \rho_1^\sigma(x, t)) \, dy, & (3.1a) \\ (\rho_2^\sigma)_t(x, t) + \chi_2 \nabla \cdot (\rho_2^\sigma(x, t) \nabla c(x, t)) &= \frac{v_2}{\sigma^2} \iint_{\mathbb{R}^2} \eta_\sigma(x - y) (\rho_2^\sigma(y, t) - \rho_2^\sigma(x, t)) \, dy, & (3.1b) \\ \tau c_t(x, t) = v \Delta c(x, t) + \gamma_1 \rho_1^\sigma(x, t) + \gamma_2 \rho_2^\sigma(x, t) - \zeta c(x, t). & & (3.1c) \end{aligned} \right.$$

The corresponding particle solutions for ρ_1^σ and ρ_2^σ of (3.1) are sought in the form

$$\widehat{\rho}_1(x, t) = \sum_{i=1}^{N_1} w_i^1(t) \delta(x - \mathbf{x}_i^1(t)) \quad \text{and} \quad \widehat{\rho}_2(x, t) = \sum_{i=1}^{N_2} w_i^2(t) \delta(x - \mathbf{x}_i^2(t)) \quad (3.2)$$

with $\mathbf{x}_i^1(t)$ and $\mathbf{x}_i^2(t)$ being each species particle locations, $w_i^1(t)$ and $w_i^2(t)$ their corresponding weights, and N_1 and N_2 the total number of each species particle. We denote by $\Omega_i^1(t)$ and $\Omega_i^2(t)$ the subdomains occupied by the corresponding particles.

In principle, one can apply the weighted particle method from §2 to (3.1a) and (3.1b), in which the particle locations, their weights, and sizes of the corresponding subdomains evolve in time according to (2.7). However, when the solutions of (3.1a) and (3.1b) start developing spiky structures, the particles start clustering in the regions of large chemoattractant gradient and hence, using a constant σ in (2.7) leads to an inaccurate approximation of the diffusion operator. Therefore, one has to use variable values of σ , which depend on the distance between the particles. In particular, we use $\sigma_{ij}^k = \sqrt{(|\Omega_i^k| + |\Omega_j^k|)/2}$, $k = 1, 2$, so that the system (2.7) for ρ_1 and ρ_2 reads as

$$\left\{ \begin{aligned} \frac{d}{dt} \mathbf{x}_i^k &= (u_i^k, v_i^k)^\top, \quad k = 1, 2, \\ \frac{d}{dt} w_i^k &= v_k \sum_{j=1}^{N_k} \frac{1}{(\sigma_{ij}^k)^2} \eta_{\sigma_{ij}^k}(\mathbf{x}_i^k - \mathbf{x}_j^k) [w_j^k |\Omega_i^k| - w_i^k |\Omega_j^k|], \quad k = 1, 2, \\ \frac{d}{dt} |\Omega_i^k| &= r_i^k |\Omega_i^k|, \quad k = 1, 2. \end{aligned} \right. \quad (3.3)$$

Here, $(u_i^k, v_i^k)^\top \approx \chi_k \nabla c(x_i^k(t), y_i^k(t), t)$ and $r_i^k \approx \chi_k \Delta c(x_i^k(t), y_i^k(t), t)$, which will be obtained in §3.3.1 below. Notice that all of the indexed quantities in (3.3) depend on t , but we have omitted this dependence for brevity. Time dependence of indexed quantities will also be omitted below unless it is necessary to emphasize it in the discussion context.

It should be observed that choosing variable σ_{ij}^k is not sufficient to make numerical integration of the ODE system (3.3) practically feasible as the time-step restriction (2.10) would lead to $\Delta t \rightarrow 0$, when ρ_1 and ρ_2 approaching the point mass concentration.

In order to overcome this difficulty, we present a new sticky particle method for the chemotaxis equations (1.1a) and (1.1b). The basic idea of sticky particle methods is to coalesce clustering particles into a “heavier” particle located at their center of mass. In this paper, we introduce a new particle merger strategy, which is implemented in two steps. Namely, at each time level t , we first identify pairs of particles whose trajectories are about to intersect by the next time level $t + \Delta t$ and merge them before the time evolution step. We then evolve the particles from t to $t + \Delta t$ and coalesce those particles, which have clustered upon the completion of the evolution step (the second merger step was used in [7, 13, 16, 18, 22]).

In order to implement the merger, we introduce an auxiliary “merger” Cartesian grid consisting of small cells of the size about $\frac{1}{4} \min_i |\Omega_i(0)|$ and assume that at a certain time level t no “merger” cell contain more than one particle. We then compute the time-step Δt based on the two-species version of the time-step restrictions (2.11)–(2.13), but not (2.10), which, as we have mentioned, may be impractically too restrictive. Equipped with this Δt , we proceed with the following steps.

Merger Step 1. We identify those pairs of the same species particles whose trajectories are about to intersect before time $t + \Delta t$. Let us assume that $\{(x_i^k, w_i^k, |\Omega_i^k|), (x_j^k, w_j^k, |\Omega_j^k|)\}$ is one of such pairs ($k = 1$ or 2), that is, $\tau_i^k > 0$, $\tau_j^k > 0$, and $\max\{\tau_i^k, \tau_j^k\} < \Delta t$, where τ_i^k and τ_j^k are given by the two-species version of (2.9). We then add the weights of these two particles, combine their subdomains, and replace the two particles with one heavier particle located at the center of mass of the replaced particles:

$$\left\{ (x_i^k, w_i^k, |\Omega_i^k|), (x_j^k, w_j^k, |\Omega_j^k|) \right\} \longrightarrow (\tilde{x}^k, \tilde{w}^k, |\tilde{\Omega}^k|)$$

with

$$\tilde{x}^k = \frac{w_i^k x_i^k + w_j^k x_j^k}{w_i^k + w_j^k}, \quad \tilde{w}^k = w_i^k + w_j^k, \quad |\tilde{\Omega}^k| = |\Omega_i^k| + |\Omega_j^k|.$$

Once the i -th and j -th particles of species k have been merged, the total number of particles for this species reduces by one, the remaining particles are re-numbered, and Merger Step 1 is repeated for each species to ensure that no particle trajectories intersect within the current time-step.

Remark 3.1 Notice that the process of searching for pairs of particles with potentially intersecting trajectories is computationally expensive if performed straightforwardly —looping through all particle pairs of species k is $\mathcal{O}(N_k^2)$ expensive. However, the search mechanism can be made efficient by introducing another auxiliary Cartesian grid with cells of size $\min_i |\Omega_i(0)|$ and using the fact that the time-step restriction (2.13) ensures that particles cannot propagate too far within one time-step. One can then check the particles located in nearby auxiliary cells. This alternative implementation is only $\mathcal{O}(N_k)$ expensive for $k = 1, 2$.

Time Evolution. The particle solution is evolved from time t to $t + \Delta t$ by numerically solving (3.3). Recall that the system (1.1) is solved subject to the homogeneous Neumann boundary conditions, which imply that no particles should leave the computational domain Ω . This is, however, not automatically guaranteed, and we, therefore, develop a “pull-back” strategy of relocating the outside particles back on the domain boundary $\partial\Omega$ as follows: we move the outside particle to the closest point on $\partial\Omega$. Once all evolved particles are located

in Ω , one has to coalesce the clustering particles according to Merger Step 2, which will be introduced shortly.

If a Runge-Kutta ODE solver is employed (as in all of the numerical experiments presented in §4), then both “pull-back” and merger algorithms should be implemented at the end of each Runge-Kutta stage.

Merger Step 2. We find all of the auxiliary “merger” cells containing more than one particle from the same species and then merge them according to the following procedure. Let C_{mer} be one of such cells with two or more particles of species k ($k = 1$ or 2). Then, the particles of species k located in C_{mer} are merged into a new particle, $(\tilde{\mathbf{x}}^k, \tilde{w}^k, |\tilde{\Omega}^k|)$, located at the center of mass of the replaced particles and their weights and subdomain sizes are summed up:

$$\tilde{\mathbf{x}}^k = \frac{\sum_{i:\mathbf{x}_i^k \in C_{\text{mer}}} w_i^k \mathbf{x}_i^k}{\sum_{i:\mathbf{x}_i^k \in C_{\text{mer}}} w_i^k}, \quad \tilde{w}^k = \sum_{i:\mathbf{x}_i^k \in C_{\text{mer}}} w_i^k, \quad |\tilde{\Omega}^k| = \sum_{i:\mathbf{x}_i^k \in C_{\text{mer}}} |\Omega_i^k|.$$

Remark 3.2 We would like to point out that, by construction, the sticky particle method preserves the positivity of ρ_1 and ρ_2 , which is a crucial property for the stability of numerical methods for PKS-type systems, as it was shown in [12].

3.2 Finite-Difference Scheme for Equation (1.1c)

In this section, we describe the second ingredient of our hybrid method—the FD scheme, which is used to numerically solve the chemoattractant concentration equation (1.1c). We restrict our consideration to the case of a rectangular computational domain Ω . For general domains, one can still use FD schemes, but the treatment of boundary conditions and grid points near the boundary becomes quite delicate (this is outside the scope of the current paper).

We first split Ω into uniform rectangular cells $C_{\ell,m}$ of dimensions Δx and Δy and denote the cell centers by $\mathbf{x}_{\ell,m} = (x_{\ell,m}, y_{\ell,m})$. A second-order FD discretization of (1.1c) (or, a semi-discretization in the parabolic-parabolic case with $\tau = 1$) reads as

$$\tau \frac{d}{dt} c_{\ell,m} = \nu(\Delta c)_{\ell,m} + \gamma_1(\rho_1)_{\ell,m} + \gamma_2(\rho_2)_{\ell,m} - \zeta c_{\ell,m}, \tag{3.4}$$

where $c_{\ell,m} \approx c(\mathbf{x}_{\ell,m}, t)$, $(\rho_1)_{\ell,m} \approx (\rho_1)(\mathbf{x}_{\ell,m}, t)$, $(\rho_2)_{\ell,m} \approx (\rho_2)(\mathbf{x}_{\ell,m}, t)$, and $(\Delta c)_{\ell,m}$ is the second-order discrete Laplacian:

$$(\Delta c)_{\ell,m} = \frac{c_{\ell+1,m} - 2c_{\ell,m} + c_{\ell-1,m}}{(\Delta x)^2} + \frac{c_{\ell,m+1} - 2c_{\ell,m} + c_{\ell,m-1}}{(\Delta y)^2}. \tag{3.5}$$

If $\tau = 1$, one needs to numerically integrate the extended ODE system (3.3)–(3.4). Otherwise, if $\tau = 0$, (3.4) is a linear algebraic system with respect to $\{c_{\ell,m}\}$, which needs to be solved upon completion of each time-step (or each stage if a Runge-Kutta ODE solver is employed).

Remark 3.3 In Appendix B, we establish a-priori estimates for the discrete $\|\nabla c\|_{L^\infty(\Omega)}$ that ensure well-posedness for smooth solutions in both the parabolic-parabolic ($\tau = 1$) and parabolic-elliptic ($\tau = 0$) cases.

Remark 3.4 We stress that the computed chemoattractant concentration values $\{c_{\ell,m}\}$ will remain positive. If $\tau = 0$, the positivity follows from the diagonal dominance of the matrix of the coefficients on $\{c_{\ell,m}\}$ in the corresponding linear system. If $\tau = 1$, then one would need first to consider the forward Euler discretization of (3.4), which will be positivity-preserving provided the following restriction on the time-step,

$$\Delta t \leq \frac{1}{\zeta + 2\nu \left(\frac{1}{(\Delta x)^2} + \frac{1}{(\Delta y)^2} \right)}, \quad (3.6)$$

is satisfied. A similar conclusion can be drawn for a high-order SSP Runge-Kutta or multistep explicit method [28, 29].

3.3 Projection Between the Particle and Grid Data

It should be observed that one has to project the data from/to the particle locations \mathbf{x}_i^k to/from the grid nodes $x_{\ell,m}$ when a meshless particle method is combined with a grid-based FD scheme. We introduce these mapping procedures in §3.3.1 and §3.3.2.

3.3.1 Computation of ∇c and Δc at Particle Locations

In order to evolve particles in time according to (3.3), one has to compute velocities $(u_i^k, v_i^k)^\top$ and their divergences r_i^k at the particle locations. Since these quantities are obtained using ∇c and Δc , and since the values $c_{\ell,m}$ are computed at the grid points, a projection of the grid data on the particle location has to be carried out.

To this end, we use the second-order FD formulae

$$(c_x)_{\ell,m} = \frac{c_{\ell+1,m} - c_{\ell-1,m}}{2\Delta x}, \quad (c_y)_{\ell,m} = \frac{c_{\ell,m+1} - c_{\ell,m-1}}{2\Delta y},$$

and the second-order discrete Laplacian (3.5) to construct global (in space) piecewise linear interpolants for c_x , c_y , and Δc , which are in every cell $C_{\ell,m}$ defined by

$$\begin{aligned} \tilde{c}_x(x, y) &= (c_x)_{\ell,m} + \frac{(c_x)_{\ell+1,m} - (c_x)_{\ell-1,m}}{2\Delta x} (x - x_{\ell,m}) + \frac{(c_x)_{\ell,m+1} - (c_x)_{\ell,m-1}}{2\Delta y} (y - y_{\ell,m}), \\ \tilde{c}_y(x, y) &= (c_y)_{\ell,m} + \frac{(c_y)_{\ell+1,m} - (c_y)_{\ell-1,m}}{2\Delta x} (x - x_{\ell,m}) + \frac{(c_y)_{\ell,m+1} - (c_y)_{\ell,m-1}}{2\Delta y} (y - y_{\ell,m}), \\ \tilde{\Delta c}(x, y) &= (\Delta c)_{\ell,m} + \frac{(\Delta c)_{\ell+1,m} - (\Delta c)_{\ell-1,m}}{2\Delta x} (x - x_{\ell,m}) \\ &\quad + \frac{(\Delta c)_{\ell,m+1} - (\Delta c)_{\ell,m-1}}{2\Delta y} (y - y_{\ell,m}). \end{aligned}$$

Finally, at each particle location \mathbf{x}_i^k , $k = 1, 2$, we obtain

$$u_i^k = \chi_k \tilde{c}_x(x_i^k, y_i^k), \quad v_i^k = \chi_k \tilde{c}_y(x_i^k, y_i^k), \quad r_i^k = \chi_k \tilde{\Delta c}(x_i^k, y_i^k). \quad (3.7)$$

3.3.2 Computation of ρ_1 and ρ_2 at Grid Points

In order to evolve c in time according to (3.4), one has to recover the density grid values $(\rho_1)_{\ell,m}$ and $(\rho_2)_{\ell,m}$ from the particle distributions (3.2). This can be conducted in the following two steps.

Step 1. For each particle satisfying $\mathbf{x}_i^k \in C_{\ell,m}$, we compute the distance from this particle to the cell center $\mathbf{x}_{\ell,m}$:

$$(d_i^k)_{\ell,m} := |\mathbf{x}_i^k - \mathbf{x}_{\ell,m}|, \tag{3.8}$$

and evaluate the grid values of ρ_1 and ρ_2 at the cell center $\mathbf{x}_{\ell,m}$ using a distance-based weighted averaging:

$$(\rho_k)_{\ell,m}^* = \frac{\sum_{\mathbf{x}_i^k \in C_{\ell,m}} \frac{w_i^k}{|\Omega_i^k|} \cdot \frac{1}{(d_i^k)_{\ell,m}}}{\sum_{\mathbf{x}_i^k \in C_{\ell,m}} \frac{1}{(d_i^k)_{\ell,m}}}, \quad k = 1, 2, \tag{3.9}$$

where $w_i^k/|\Omega_i^k|$ are the point values of ρ_k at the particle locations \mathbf{x}_i^k . If there is no particles of species k in cell $C_{\ell,m}$, we set $(\rho_k)_{\ell,m}^* = 0$.

Step 2. In the cells containing no particles, the value $(\rho_k)_{\ell,m}^* = 0$ may be very inaccurate. We, therefore, replace the values computed in **Step 1** with

$$(\rho_k)_{\ell,m} = \begin{cases} (\rho_k)_{\ell,m}^* & \text{if } \exists i : \mathbf{x}_i^k \in C_{\ell,m}, \\ \frac{(\rho_k)_{\ell+1,m}^* + (\rho_k)_{\ell-1,m}^* + (\rho_k)_{\ell,m+1}^* + (\rho_k)_{\ell,m-1}^*}{4 + 2\sqrt{2}} & \text{otherwise.} \\ + \frac{(\rho_k)_{\ell+1,m+1}^* + (\rho_k)_{\ell+1,m-1}^* + (\rho_k)_{\ell-1,m+1}^* + (\rho_k)_{\ell-1,m-1}^*}{4 + 4\sqrt{2}} & \end{cases}$$

where the latter expression is the distance-based weighted averaging over neighboring cells.

Remark 3.5 It should be observed that there are other ways to recover grid values of the computed solution from its particle distribution when the solution is smooth; see, e.g., [6]. However, after the spiky structure is developed, most of these methods are based on a certain regularization of the δ -functions, leading to a substantial decrease of the maximum values of ρ_1 and ρ_2 . The method we introduced above seems to be the only robust option.

Remark 3.6 Note that some of the values d_i^k defined in (3.8) may be very small or even zero. We, therefore, need to desingularize the computation in (3.9) to prevent division by small numbers. This is done by replacing (3.8) with

$$(d_i^k)_{\ell,m} = \max \left\{ d_{\min}, |\mathbf{x}_i^k - \mathbf{x}_{\ell,m}| \right\},$$

where d_{\min} is a small positive number taken to be $\min(\Delta x, \Delta y)/16$ in all of the numerical examples reported in §4.

3.4 Summary of the Numerical Algorithm

Before demonstrating the performance of the proposed hybrid FDP method, we summarize our approach using the following algorithm.

Algorithm 3.1. Hybrid Finite-Difference-Particle Method

Data: The studied chemotaxis system subject to the initial conditions.

Step 1: Introduce the required three different meshes for distinct purposes: a mesh used in the FD scheme ($C_{\ell,m}$), a mesh used as initial particle subdomains $\Omega_i(0)$, and a mesh used for Merger Step 2 (C_{mer}).

Step 2: Use a particle approximation described in §2 and §3.1 to initialize the particle approximations of the cell densities ρ_1 and ρ_2 . Initialize point values of the chemoattractant concentration c ; see §3.2.

Step 3: Identify particle trajectories and use the particle Merger Step 1 described in §3.1.

Step 4: Compute the point values ρ_1 and ρ_2 at the FD grid points according to §3.3.2.

Step 5: Compute the point values of c_x , c_y , and Δc at the particle locations according to §3.3.1.

Step 6 (Parabolic-Parabolic Case): Use the three-stage third-order SSP Runge-Kutta method to evolve the particles by numerically solving (3.3) and the point-values of c by numerically solving (3.4). Use the “pull-back” strategy to relocate the outside particles back on $\partial\Omega$.

Step 6 (Parabolic-Elliptic Case): Use the three-stage third-order SSP Runge-Kutta method to evolve the particles by numerically solving (3.3). Use the “pull-back” strategy to relocate the outside particles back on $\partial\Omega$. Solve the elliptic equation (3.4) to update the point-values of c .

Step 7: Use the particle Merger Step 2 described in §3.1.

if reach the final time t then

 | stop;

else

 | go back to Step 3;

end

Result: Numerical solution of the studied chemotaxis system.

4 Numerical Examples

In this section, we demonstrate the performance of the proposed hybrid FDP method and its capability of capturing the blowing-up solutions of the PKS-type system (1.1) with high resolution.

Recall that the proposed method employs three different meshes; see Algorithm 3.1. In the following numerical examples, we use uniform meshes with $\Delta := \Delta x = \Delta y$ and keep the ratio between these three mesh sizes fixed. Specifically, by “numerical results obtained on a mesh of size Δ ”, we imply the combination of a mesh of size Δ for the FD scheme, a mesh of size $\Delta/4$ for initial particle subdomains, and a mesh of size $\Delta/8$ for the merger.

For time evolution, we use the three-stage third-order SSP Runge-Kutta method [28, 29]. The time-step is selected using the stability restrictions introduced in (2.11)–(2.13). We remind the reader that once the final time solution has been computed, the point values of c are available, while the point values of ρ_1 and ρ_2 need to be recovered as described in **Steps 1 and 2** in §3.3.2. In order to visualize the obtained solution and conduct the experimental convergence study, one may use, for instance, the MATLAB built-in function `scatteredInterpolant`.

It is instructive also to monitor the time evolution of the free energy, which should be decaying for smooth solutions in both single- and two-species cases; see, e.g., [1, 3, 31, 45] and references therein. For completeness, in Appendix A, a derivation of the free energy formula and the proof of its decay are provided in a more challenging two-species case. It should be observed that the free energy decay is not guaranteed for the proposed hybrid FDP method (unlike the provably energy-decaying methods in, e.g., [1, 3, 31, 45]), but we focus on a lower dissipative approach allowing one to more accurately capture blowing up solutions, especially in the two-species case (see Examples 2 and 5).

4.1 Parabolic-Parabolic Case ($\tau = 1$)

Example 1—Accuracy Test

The primary objective of this example is to check the accuracy of the proposed hybrid FDP method experimentally.

We consider the system (1.1) with $\tau = 1$, $\nu = 10$, $\chi_1 = 5$, $\chi_2 = 60$, $\gamma_1 = \gamma_2 = \zeta = \nu_1 = \nu_2 = 1$, and subject to the following initial conditions:

$$\begin{aligned} \rho_1(x, y, 0) = \rho_2(x, y, 0) &= 500 e^{-100(x^2+y^2)}, & c(x, y, 0) &\equiv 1, \\ (x, y) \in \Omega &= [-1, 1] \times [-1, 1]. \end{aligned}$$

We compute the numerical solutions until time $t = 2 \times 10^{-4}$ using various resolutions with $\Delta = 2/15, 2/20, 2/25, 2/30, 2/40, 2/50, 2/60, 2/80, 2/100$, and $2/120$. Given the numerical solutions obtained on meshes of sizes $\Delta, 2\Delta$, and 4Δ , we compute the L^1 - and L^2 -errors and estimate the corresponding experimental convergence rates using the following Runge formulae:

$$L^p\text{-error} \approx \frac{\|(\cdot)^{2\Delta} - (\cdot)^\Delta\|_{L^p}^2}{\|(\cdot)^{4\Delta} - (\cdot)^{2\Delta}\|_{L^p} - \|(\cdot)^{2\Delta} - (\cdot)^\Delta\|_{L^p}}, \quad \text{rate} \approx \log_2 \left(\frac{\|(\cdot)^{4\Delta} - (\cdot)^{2\Delta}\|_{L^p}}{\|(\cdot)^{2\Delta} - (\cdot)^\Delta\|_{L^p}} \right), \quad p = 1, 2,$$

where $(\cdot)^\Delta$ denotes the numerical results obtained on a mesh of size Δ .

The computed L^1 - and L^2 -errors and the corresponding experimental convergence rates for ρ_1, ρ_2 , and c are presented in Table 1, where one can see that the second order of accuracy is achieved.

Example 2—Two-Species Blowup at the Center of the Domain

In this example, we consider the same initial-boundary value problem (IBVP) as in Example 1 but compute its numerical solution until much larger times $t = 5 \times 10^{-4}$ and 10^{-3} . The densities ρ_1 and ρ_2 obtained on a mesh of size $\Delta = 1/20$ are plotted in Figure 1. The results are comparable to the ones in [15, Example 3] and [37]: Both ρ_1 and ρ_2 exhibit blowup behavior, and the solution of ρ_2 blows up faster.

Table 1 Example 1: The L^1 - and L^2 -errors and the corresponding convergence rates

Δ	ρ_1			ρ_2			c					
	L^1 -error	rate	L^2 -error	rate	L^1 -error	rate	L^2 -error	rate	L^1 -error	rate	L^2 -error	rate
2/60	2.94e-2	1.95	1.35e-1	1.88	7.70e-2	2.20	2.94e-1	2.43	1.80e-4	1.78	4.12e-4	2.00
2/80	1.55e-2	2.00	7.75e-2	1.85	4.52e-2	1.64	1.96e-1	1.70	1.06e-4	1.81	3.43e-4	1.65
2/100	1.04e-2	1.93	4.48e-2	1.93	2.19e-2	2.43	8.40e-2	2.68	7.33e-5	1.75	1.65e-4	1.93
2/120	6.20e-3	2.07	2.55e-2	2.10	1.93e-2	2.11	6.63e-2	2.06	4.52e-5	1.87	1.06e-4	1.99

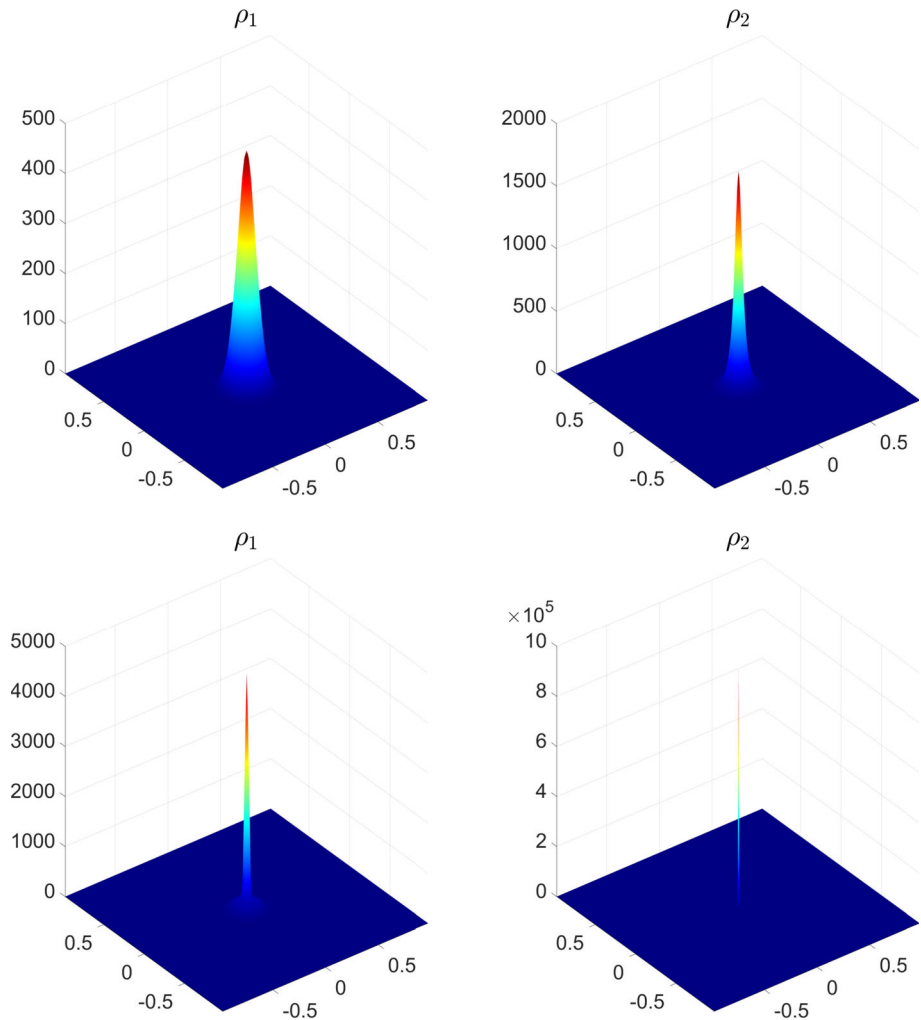


Fig. 1 Example 2: $\rho_1(x, 0.0005)$ (upper left), $\rho_2(x, 0.0005)$ (upper right), $\rho_1(x, 0.001)$ (lower left), and $\rho_2(x, 0.001)$ (lower right), obtained using the hybrid FDP method with $\Delta = 1/20$

This example is challenging in the sense that excessive numerical viscosity may smear the singularity, leading to a failure to capture the blowup behavior. Due to the low-dissipation nature of the sticky particle method, the hybrid FDP method provides a higher resolution: The maximum values of ρ_1 and ρ_2 are respectively 4.7355×10^3 and 9.6558×10^5 , as compared to 3.5758×10^3 and 2.8726×10^5 reported in [15, Example 3].

We also monitor the time evolution of the discrete energy; see Figure 2 (left), where one can see that the energy is decaying and the rate of decay sharply increases after the solution gradients start sharply increasing.

We remind the reader that the time-step in our numerical simulations is selected adaptively as described in §2. It should be observed that at the initial stages of the solution evolution (when $|\nabla c|$ is relatively small; recall that $(u^k, v^k)^\top = \chi_k \nabla c$, $k = 1, 2$), the time-step restriction is mainly affected by the diffusion terms, that is, by (3.6). However, as the solution

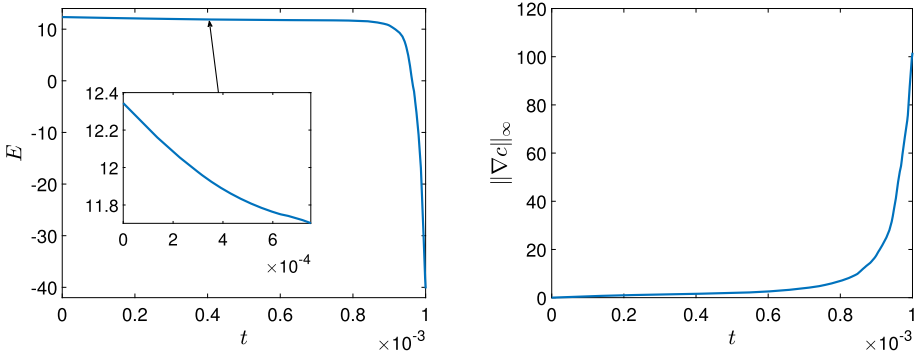


Fig. 2 Example 2: Temporal evolution of E (left) and $\|\nabla c\|_\infty$ (right)

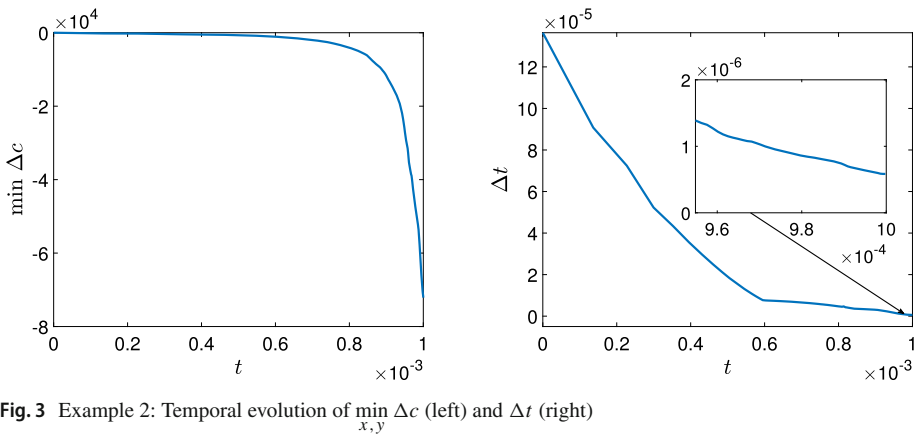


Fig. 3 Example 2: Temporal evolution of $\min \Delta c$ (left) and Δt (right)

evolves, the system transitions to a convection-dominated regime since $|\nabla c|$ grows in certain regions and the particle velocities significantly increase (see Figure 2 (right), where we plot $\|\nabla c\|_\infty$ as a function of time), resulting in a substantial decrease in the size of time-steps, which are also affected by the decrease of $\nabla \cdot \mathbf{u}^k = \chi_k \Delta c$, $k = 1, 2$; see Figure 3 (left). A temporal evolution of the time-steps is plotted in Figure 3 (right). As one can see, while the time-step decreases by a factor of more than 100 from its initial value, it does not approach zero thanks to the particle merger strategies, which prevent the particles from clustering too closely. We would also like to emphasize that particle merger together with the decrease of Ω_i^k for those particles in which the mass is accumulated, lead to the continuous in time increase of both $\|\rho_1\|_\infty$ and $\|\rho_2\|_\infty$ as shown in Figure 4.

Example 3—Single-Species Blowup at the Corner of the Domain

The third example taken from [12] is designed to demonstrate the ability of the proposed hybrid FDP method to capture the blowup behavior away from the center of the initial Gaussian-shaped cell density.

We consider the single-species PKS system

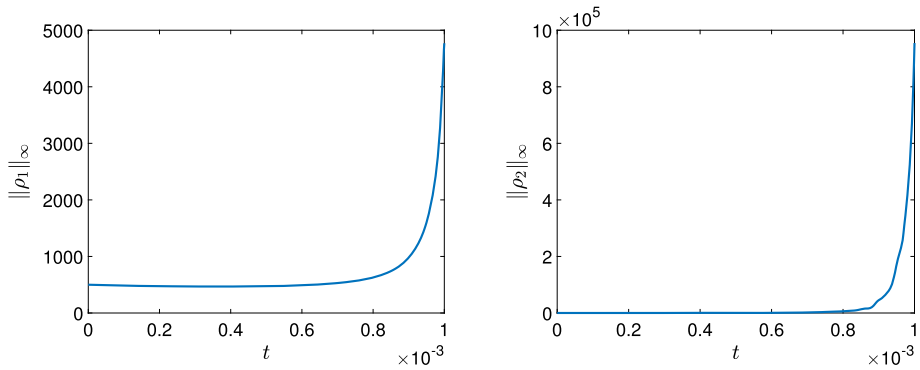


Fig. 4 Example 2: Temporal evolution of $\|\rho_1\|_\infty$ (left) and $\|\rho_2\|_\infty$ (right)

$$\begin{cases} \rho_t + \nabla \cdot (\rho \nabla c) = \Delta \rho, \\ c_t = \Delta c + \rho - c, \end{cases} \tag{4.1}$$

subject to the following initial conditions:

$$\begin{aligned} \rho(x, y, 0) &= 500 e^{-100[(x-0.25)^2+(y-0.25)^2]}, \quad c(x, y, 0) \equiv 0, \\ (x, y) \in \Omega &= [-0.5, 0.5] \times [-0.5, 0.5]. \end{aligned} \tag{4.2}$$

It has been proved in [33] that when the total mass of ρ is below a certain threshold, the density ρ can only blow up at the boundary of the computational domain. This is indeed the case for the IBVP (4.1)–(4.2).

We employ the hybrid FDP method to compute the solution on a mesh of size $\Delta = 1/20$. The density ρ at different times is shown in Figure 5, and the particle locations $\{(x_i(t), y_i(t))\}$ at times $t = 0.02$ and 0.1 are depicted in Figure 6. As one can observe, the behavior of the computed solution matches the theoretical results established in [33]: The mass of ρ first moves to the boundary and then concentrates at the corner where the solution blows up.

Example 4—Single-Species Blowup in the Interior of the Domain

We consider the same IBVP as in Example 3, but with different initial conditions:

$$\begin{aligned} \rho(x, y, 0) &= 1000 e^{-100[(x-0.25)^2+(y-0.25)^2]}, \quad c(x, y, 0) \equiv 0, \\ (x, y) \in \Omega &= [-0.5, 0.5] \times [-0.5, 0.5]. \end{aligned}$$

In this case, the total mass of ρ is greater than the threshold, and the solution may blow up in the interior of the computational domain.

We compute the solution by the proposed hybrid FDP method on a mesh of size $\Delta = 1/20$ until the final time $t = 0.1$. In Figure 7, we plot the density ρ at different times together with the location of the “dominating” particle at $t = 0.1$ (by that time, the solution has blown up and most of the mass is concentrated at the “dominating” particle), which is, as one can clearly see, inside the domain. This result is consistent with both the theoretical result in [33] and the numerical results reported in [2, 14].

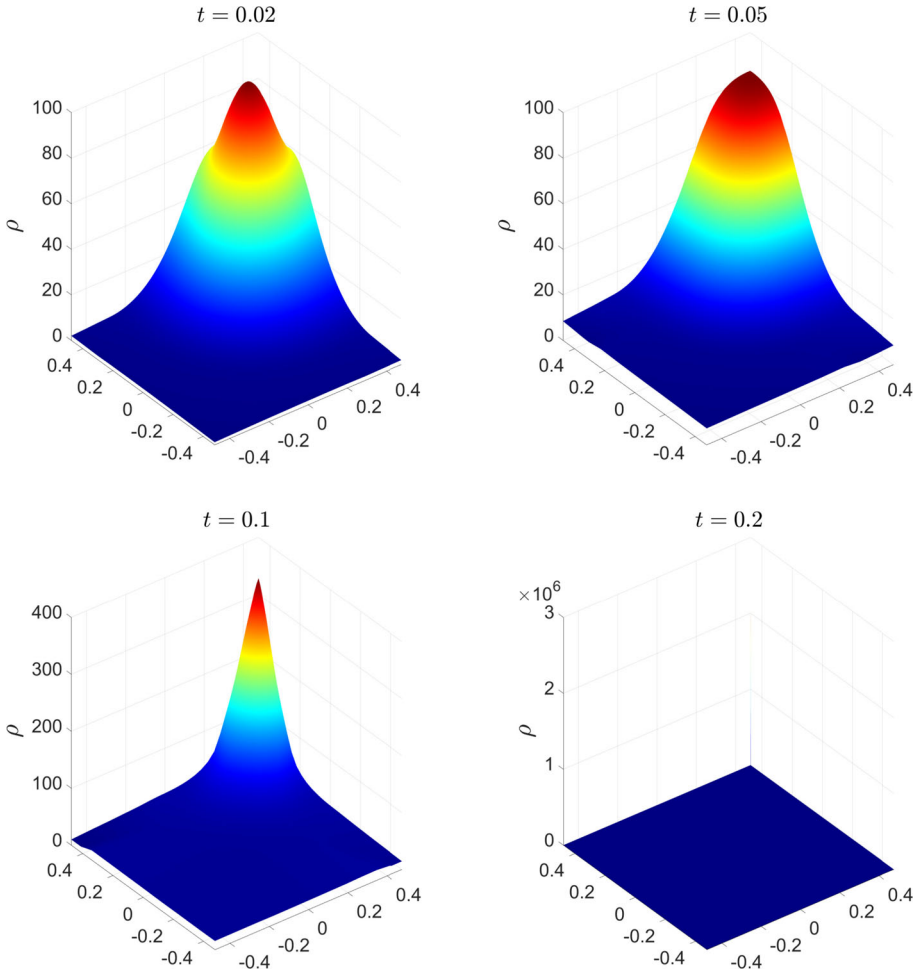


Fig. 5 Example 3: $\rho(x, 0.02)$ (upper left), $\rho(x, 0.05)$ (upper right), $\rho(x, 0.1)$ (lower left), and $\rho(x, 0.2)$ (lower right), obtained using the hybrid FDP method with $\Delta = 1/20$

4.2 Parabolic-Elliptic Case ($\tau = 0$)

In this section, we consider an extremely challenging numerical example introduced in [37].

Example 5—Two-Species Blowup at the Center of the Domain

In this example, we consider the system (1.1) with $\tau = 0$, $\gamma_1 = \gamma_2 = \zeta = \nu_1 = \nu_2 = \nu = \chi_1 = 1$, $\chi_2 = 20$, and subject to the following initial conditions:

$$\rho_1(x, y, 0) = \rho_2(x, y, 0) = 50 e^{-100(x^2+y^2)}, \quad (x, y) \in \Omega = [-1, 1] \times [-1, 1].$$

According to [26, 27], both ρ_1 and ρ_2 are expected to blow up *simultaneously* in finite time. However, as demonstrated in [10, 15, 37], ρ_1 and ρ_2 are expected to undergo different blowup patterns: While ρ_2 develops a δ -type singularity, ρ_1 grows up algebraically.

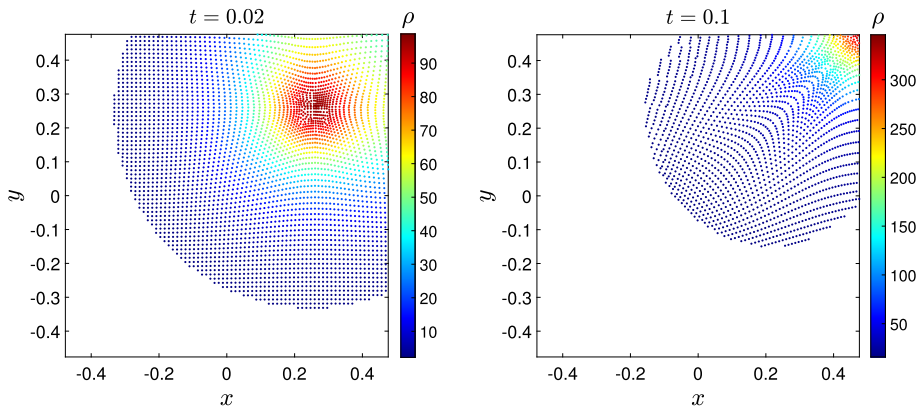


Fig. 6 Example 3: Particle locations at $t = 0.02$ (left) and $t = 0.1$ (right), obtained using the hybrid FDP method with $\Delta = 1/20$. The color indicates the value of $w_i(t)/|\Omega_i(t)|$

We compute the solution until the same (as in [10, 15, 37]) final time $t = 0.0033$ using the proposed hybrid FDP method on a mesh of size $1/20$. The densities ρ_1 and ρ_2 , obtained at times $t = 0.003$ and 0.0033 are shown in Figure 8. We would like to emphasize that achieving a high resolution of blowup behavior in ρ_1 is a particularly challenging task. Neither the second-order hybrid finite-volume-finite-difference [37] nor its fourth-order version [10] were able to capture the algebraic blowup of ρ_1 . Some improvement was achieved in [15], where an AMM finite-volume upwind method was developed and applied to the studied IBVP, but the maximum of the blown up ρ_1 on the finest mesh there was about 75 (compare with the corresponding maximum of ρ_2 , which was about 1.3×10^5). One can observe in Figure 8, our hybrid FDP method leads to a considerably higher resolution of ρ_1 compared to the schemes in [10, 15, 37]: The maximum values of ρ_1 and ρ_2 at $t = 0.0033$ are about 6.2×10^4 and 1.6×10^5 , respectively. The significant improvement in the resolution of ρ_1 is attributed to the low-dissipation nature of the sticky particle method.

In Figure 9, we present time evolution of the maximum values of ρ_1 and ρ_2 for $\Delta = 1/15, 1/20, 1/25,$ and $1/30$. As one can see, by refining the mesh from $\Delta = 1/15$ to $1/30$, the maximum of ρ_1 increases by a factor of about 6, which exhibits a much faster increase compared to those obtained in [10, 15, 37]. This clearly demonstrates that the hybrid FDP method outperforms its grid-based counterparts in accurately capturing blowup behaviors. We would also like to point out that the maximum of ρ_2 does not increase after the predicted blowup time. This is attributed to the fact that by that time, most of the mass of the second species had been already concentrated at the origin; see Figure 10, where we plot the particle locations $\{(x_i^k(t), y_i^k(t))\}, k = 1, 2$ at times $t = 0.003$ and 0.0033 . We note that due to the particle merger, the total number of particles is decreasing in time: while initially there were $N_1 = N_2 = 3705$ particles, at $t = 0.003$ and $0.0033, N_1 = 3447$ and 1963 , respectively. At the same time, $N_2 = 1$ at both times, that is, by $t = 0.003$ all of the second species particles have already merged into a single particle. It is also instructive to see N_1 and N_2 as functions of time, which we plot in Figure 11.

It should also be observed that the blowup time for the PKS-type system (1.1) cannot be obtained theoretically, and therefore it is important to determine it numerically. Figure 9 suggests that the solution computed by the hybrid FDP method blows up by time $t = 0.00294$, at which the entire mass of the second species concentrates at one point (noticeably, this time is the same for different Δ). This is demonstrated by zooming in on the peak curves in

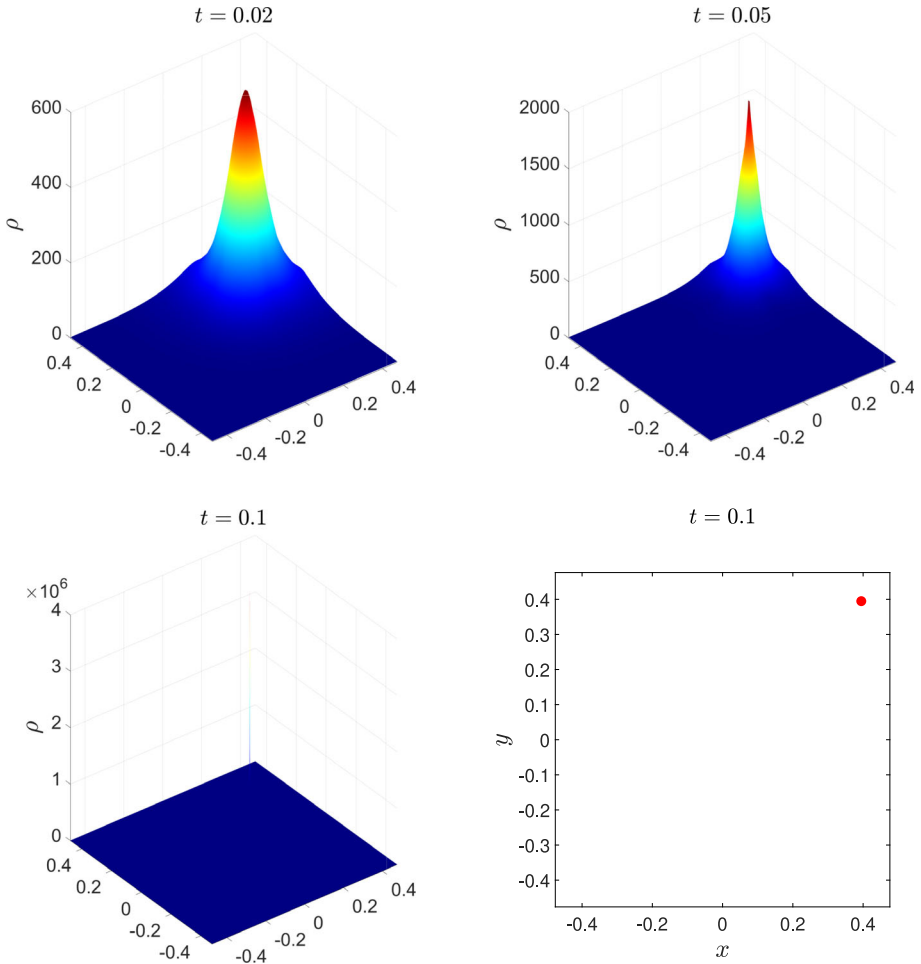


Fig. 7 Example 4: $\rho(x, 0.02)$ (upper left), $\rho(x, 0.05)$ (upper right), $\rho(x, 0.1)$ (lower left), and the location of the “dominating” particle at $t = 0.1$ (lower right), obtained using the hybrid FDP method with $\Delta = 1/20$

Figure 9 within the time interval $[0.028, 0.003]$, allowing for a clearer comparison between the blowup behavior of the first and second species. We note that the observed blowup time ($t = 0.00294$) is smaller than the one ($t = 0.0033$) reported in [15]; see also [10, 37]. This is attributed to the low-dissipation nature of the sticky particle method compared to the grid-based methods in [10, 15, 37], which contain a much larger amount of numerical dissipation that causes a delay in blowup for both ρ_1 and ρ_2 .

As in Example 2, we monitor the time evolution of the discrete free energy (see Figure 12 (left)), whose behavior is now very different from that observed in Example 2. First, even before the sharp increase of the solution gradients starts, the decay is clearly non-monotone, and at the blowup stage, the free energy drops drastically. The time evolution of $\|\nabla c\|_\infty$ is also similar: it first increases in not perfectly monotone way and then sharply jumps up at the predicted blowup time; see Figure 12 (right). Similarly, one can observe a non-monotone decay in the size of time-steps; see Figure 13 (right). We believe that these oscillations are

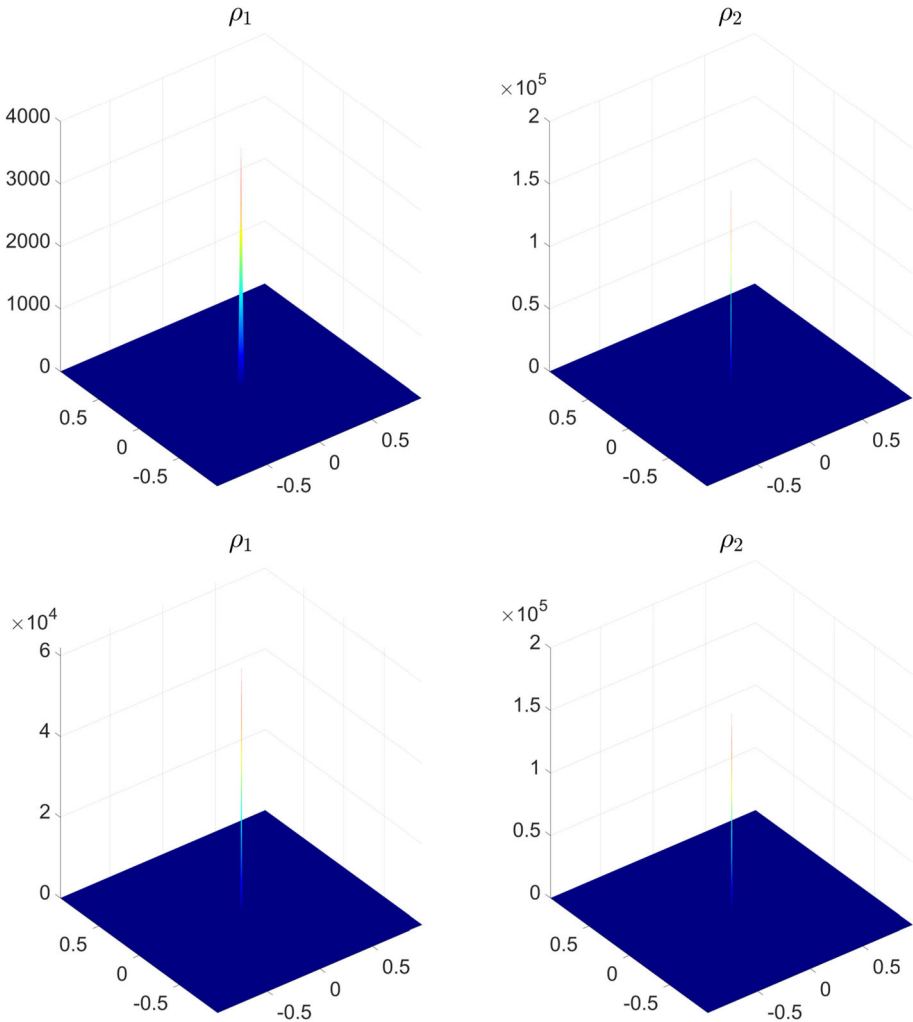


Fig. 8 Example 5: $\rho_1(x, 0.003)$ (upper left), $\rho_2(x, 0.003)$ (upper right), $\rho_1(x, 0.0033)$ (lower left), and $\rho_2(x, 0.0033)$ (lower right), obtained using the hybrid FDP method with $\Delta = 1/20$

attributed to the merger procedures, which lead to the decrease the total number of particles, increase the distance between the particles, and decrease of the area occupied by the particles, in which the mass is accumulated (the latter is correlated with the time evolution of $\min_{x,y} \Delta c$ shown in Figure 13 (left)). It should also be observed that the size of the time steps stabilizes after the blowup occurs.

5 Conclusion

In this paper, we have designed a novel hybrid finite-difference-particle (FDP) method for the Patlak-Keller-Segel-type chemotaxis systems in either parabolic-parabolic or parabolic-

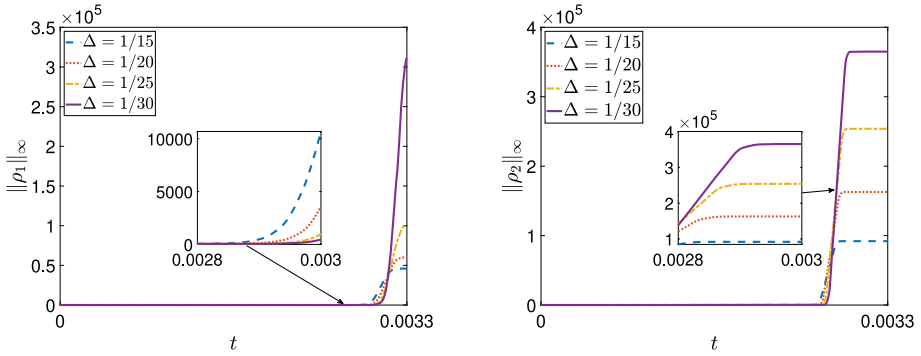


Fig. 9 Example 5: The maximums of ρ_1 (left) and ρ_2 (right) computed using $\Delta = 1/15, 1/20, 1/25,$ and $1/30$

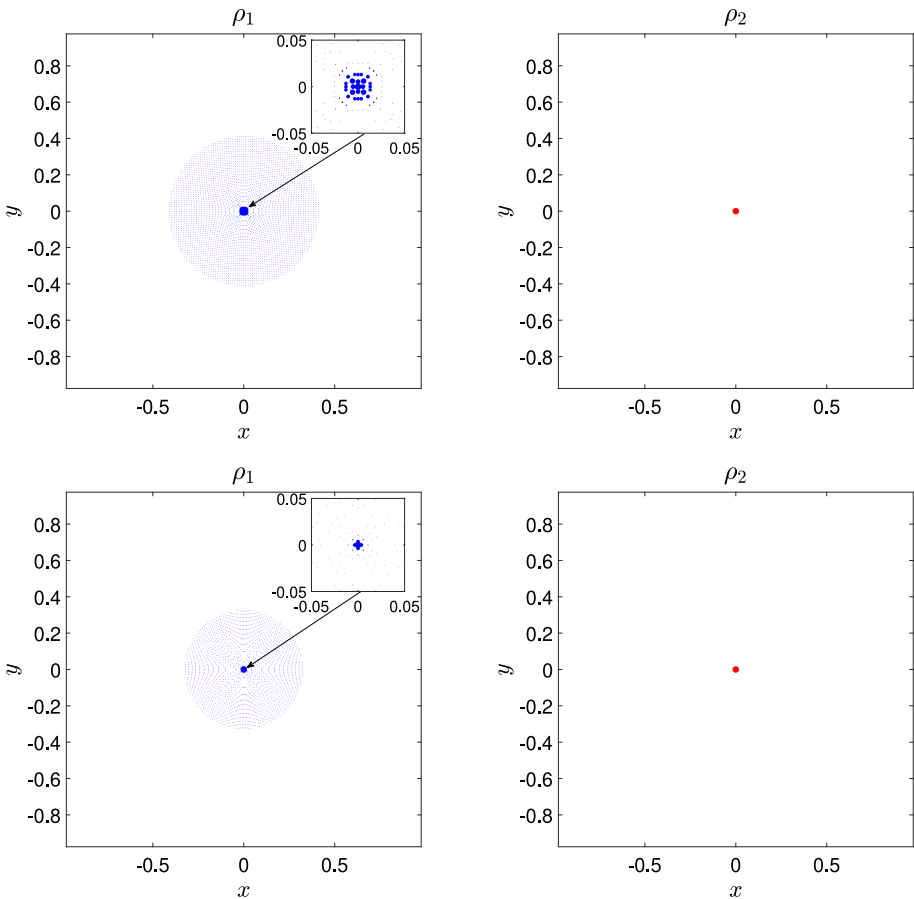


Fig. 10 Example 5: Particle locations at $t = 0.003$ (top row) and $t = 0.0033$ (bottom row) for the first (left column) and second (right column) species. The panels in the left column also contain zooms at the blowup region. Particle densities, normalized at each of the panels independently, are proportional to their radii. Note that for the entire mass of the second species has concentrated into a single particle in both panels in the right column

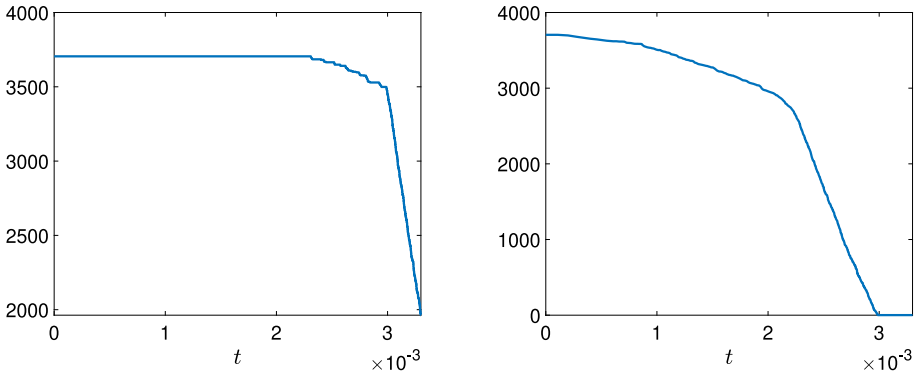


Fig. 11 Example 5: Temporal evolution of N_1 (left) and N_2 (right)

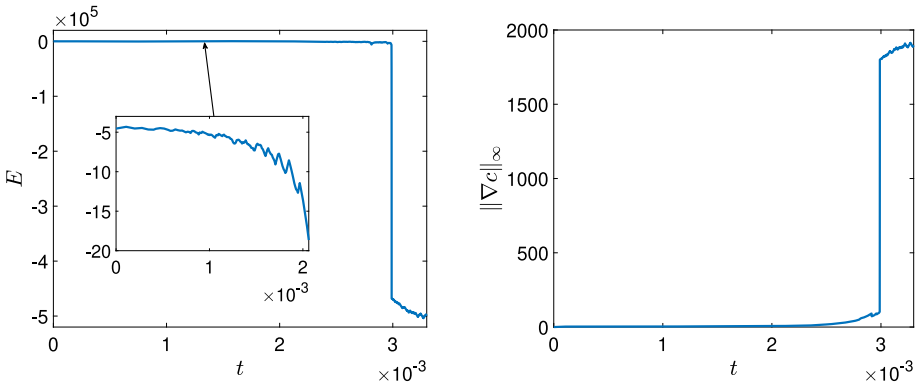


Fig. 12 Example 5: Temporal evolution of E (left) and $\|\nabla c\|_\infty$ (right)

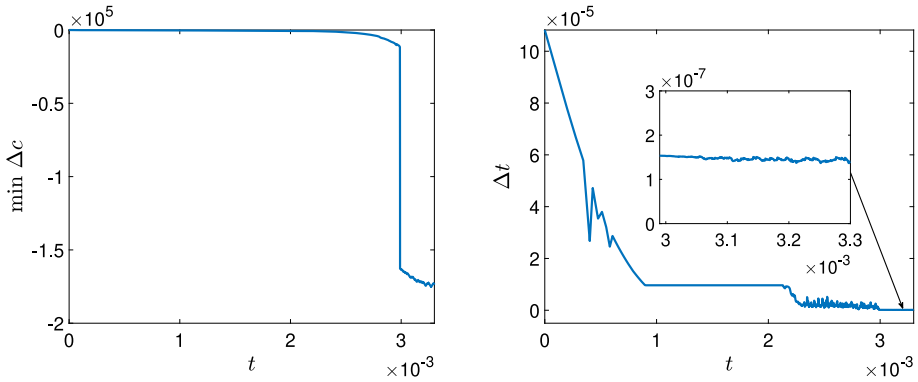


Fig. 13 Example 5: Temporal evolution of $\min_{x,y} \Delta c$ (left) and Δt (right)

elliptic form. Our approach uses a sticky particle method for the cell density equation(s) and a second-order finite-difference scheme for the chemoattractant equation. The performance of the proposed hybrid FDP methods has been examined using a comprehensive series of challenging examples. Thanks to the low-dissipation nature of the sticky particle method, the proposed scheme is particularly adept at capturing the blowing-up solutions in both one- and two-species cases. The numerical results obtained using the hybrid FDP methods exhibit superior resolution compared to traditional grid-based methods.

In our future works, we plan to extend the proposed hybrid FDP method to the two-species chemotaxis-competition models, which are even more challenging as they contain Lotka–Volterra competition terms, which require the development of special techniques to be treated within the framework of sticky particle methods. In addition, we intend to generalize the introduced method to more general (not rectangular) domains. This can be achieved by replacing the finite-difference method for the chemoattractant concentration with either a finite-volume or finite-element method capable of handling complex domains. We also note that the hybrid FDP can be extended to three-dimensional chemotaxis models relatively easily as the only difficulty related to the fact that particle trajectories may skew—the situation that does not exist in two space dimensions.

A Free Energy

In this Appendix, we derive the free energy formula for the two-species PKS type chemotaxis system (1.1) and prove its decay.

We first consider smooth solutions of (1.1) and introduce the functions

$$\mu_i := \frac{\gamma_i v_i}{\chi_i} \ln(\rho_i) - \gamma_i c, \quad i = 1, 2, \tag{A.1}$$

which can be differentiated with respect to time to obtain

$$\rho_i(\mu_i)_t = \frac{\gamma_i v_i}{\chi_i} (\rho_i)_t - \gamma_i \rho_i c_t, \quad i = 1, 2. \tag{A.2}$$

Multiplying (1.1a) and (1.1b) by μ_1 and μ_2 , respectively, integrating over Ω , and using the divergence theorem, yield for $i = 1, 2$:

$$\begin{aligned} \iint_{\Omega} \mu_i(\rho_i)_t \, dx &= \iint_{\Omega} \mu_i [v_i \Delta \rho_i - \chi_i \nabla \cdot (\rho_i \nabla c)] \, dx = - \iint_{\Omega} \nabla \mu_i \cdot (v_i \nabla \rho_i - \chi_i \rho_i \nabla c) \, dx \\ &= - \iint_{\Omega} \nabla \mu_i \cdot [v_i \rho_i \nabla (\ln(\rho_i)) - \chi_i \rho_i \nabla c] \, dx = - \frac{\chi_i}{\gamma_i} \iint_{\Omega} \rho_i |\nabla \mu_i|^2 \, dx. \end{aligned} \tag{A.3}$$

It follows from (A.2) and (A.3) that for $i = 1, 2$ we have

$$\begin{aligned} \iint_{\Omega} (\mu_i \rho_i)_t \, dx &= \iint_{\Omega} [\mu_i(\rho_i)_t + \rho_i(\mu_i)_t] \, dx \\ &= \iint_{\Omega} \left[- \frac{\chi_i}{\gamma_i} \rho_i |\nabla \mu_i|^2 + \frac{\gamma_i v_i}{\chi_i} (\rho_i)_t - \gamma_i \rho_i c_t \right] \, dx. \end{aligned} \tag{A.4}$$

Next, multiplying (1.1c) by c_t , integrating over Ω , and using the divergence theorem, yield

$$\begin{aligned} \tau \iint_{\Omega} c_t^2 \, d\mathbf{x} &= \iint_{\Omega} (v \Delta c + \gamma_1 \rho_1 + \gamma_2 \rho_2 - \zeta c) c_t \, d\mathbf{x} \\ &= \iint_{\Omega} [-v \nabla c \cdot \nabla(c_t) + (\gamma_1 \rho_1 + \gamma_2 \rho_2 - \zeta c) c_t] \, d\mathbf{x}. \end{aligned} \tag{A.5}$$

Finally, adding (A.4) for $i = 1$ and $i = 2$ and (A.5), we obtain

$$\frac{dE(t)}{dt} = - \iint_{\Omega} \left(\frac{\chi_1}{\gamma_1} \rho_1 |\nabla \mu_1|^2 + \frac{\chi_2}{\gamma_2} \rho_2 |\nabla \mu_2|^2 + \tau c_t^2 \right) \, d\mathbf{x} \leq 0,$$

where

$$E(t) := \iint_{\Omega} \left(\rho_1 \mu_1 + \rho_2 \mu_2 - \frac{\gamma_1 v_1}{\chi_1} \rho_1 - \frac{\gamma_2 v_2}{\chi_2} \rho_2 + \frac{v}{2} |\nabla c|^2 + \frac{\zeta}{2} c^2 \right) \, d\mathbf{x} \tag{A.6}$$

with μ_1 and μ_2 given by (A.1), is the free energy.

In order to monitor the time evolution of $E(t)$, one needs to discretize (A.6). Notice that the particle approximation of ρ_1 and ρ_2 cannot be substituted into (A.6) due to the presence of the terms $\rho_i \ln(\rho_i)$, $i = 1, 2$ there. We therefore use the grid values of c , ρ_1 , and ρ_2 (the latter ones are obtained in §3.3.2) and approximate the integral in (A.6) using the midpoint rule combined with the second-order FD approximations of the derivatives of ∇c .

B Appendix

In this section, we provide a more detailed description of the numerical solution of (3.4) in both the parabolic-parabolic ($\tau = 1$) and parabolic-elliptic ($\tau = 0$) cases and prove the following theorem, which establishes a-priori estimates for the discrete $\|\nabla c\|_{L^\infty(\Omega)}$ (hereafter, $\|\cdot\|_\infty := \|\cdot\|_{L^\infty(\Omega)}$) and ensures well-posedness for smooth solutions.

Theorem B.1 *Assume that $\|\nabla \rho_i\|_\infty \leq C_1$, $i = 1, 2$ for all $t \leq T$ and the initial data $c(x, 0)$ satisfies $\|\nabla c(\cdot, 0)\|_\infty \leq C$, then for the discrete solution of (3.4), $\|\nabla c\|_\infty$ is bounded for all $t \leq T$ in both the parabolic-parabolic ($\tau = 1$) and parabolic-elliptic ($\tau = 0$) cases. In the former case, the theorem’s statement is true provided (3.4) is integrated using an explicit SSP ODE solver.*

Proof We will consider the parabolic-parabolic and parabolic-elliptic cases separately.

Parabolic-Parabolic Case ($\tau = 1$). Consider the ODE system (3.4) and assume that it is integrated using the forward Euler method. The fully discrete update for the chemoattractant concentration equation thus becomes:

$$\begin{aligned} c_{\ell,m}(t + \Delta t) &= \alpha_{\ell+1,m} c_{\ell+1,m}(t) + \alpha_{\ell-1,m} c_{\ell-1,m}(t) + \alpha_{\ell,m+1} c_{\ell,m+1}(t) \\ &\quad + \alpha_{\ell,m-1} c_{\ell,m-1}(t) \\ &\quad + \alpha_{\ell,m} c_{\ell,m}(t) + \Delta t \gamma_1 (\rho_1)_{\ell,m}(t) + \Delta t \gamma_2 (\rho_2)_{\ell,m}(t), \end{aligned} \tag{B.1}$$

where

$$\alpha_{\ell+1,m} = \alpha_{\ell-1,m} = \Delta t \frac{v}{(\Delta x)^2}, \quad \alpha_{\ell,m+1} = \alpha_{\ell,m-1} = \Delta t \frac{v}{(\Delta y)^2},$$

$$\alpha_{\ell,m} = 1 - \Delta t \left[\zeta + 2v \left(\frac{1}{(\Delta x)^2} + \frac{1}{(\Delta y)^2} \right) \right].$$

Taking the discrete gradient derivatives of the left- and right-hand sides of (B.1), yields the following:

$$\begin{aligned} \nabla c_{\ell,m}(t + \Delta t) &= \alpha_{\ell+1,m} \nabla c_{\ell+1,m}(t) + \alpha_{\ell-1,m} \nabla c_{\ell-1,m}(t) + \alpha_{\ell,m+1} \nabla c_{\ell,m+1}(t) \\ &\quad + \alpha_{\ell,m-1} \nabla c_{\ell,m-1}(t) \\ &\quad + \alpha_{\ell,m} \nabla c_{\ell,m}(t) + \Delta t \gamma_1 (\nabla \rho_1)_{\ell,m}(t) + \Delta t \gamma_2 (\nabla \rho_2)_{\ell,m}(t). \end{aligned}$$

Using the last equation and the restriction on the time-step in Remark 3.4, we obtain

$$\begin{aligned} \|\nabla c(\cdot, t + \Delta t)\|_\infty &\leq \alpha_{\ell+1,m} \|\nabla c(\cdot, t)\|_\infty + \alpha_{\ell-1,m} \|\nabla c(\cdot, t)\|_\infty + \alpha_{\ell,m+1} \|\nabla c(\cdot, t)\|_\infty \\ &\quad + \alpha_{\ell,m-1} \|\nabla c(\cdot, t)\|_\infty + \alpha_{\ell,m} \|\nabla c(\cdot, t)\|_\infty + \Delta t \gamma_1 \|\nabla \rho_1(\cdot, t)\|_\infty \\ &\quad + \Delta t \gamma_2 \|\nabla \rho_2(\cdot, t)\|_\infty \\ &= (1 - \Delta t \zeta) \|\nabla c(\cdot, t)\|_\infty + \Delta t \gamma_1 \|\nabla \rho_1(\cdot, t)\|_\infty + \Delta t \gamma_2 \|\nabla \rho_2(\cdot, t)\|_\infty \\ &\leq \|\nabla c(\cdot, t)\|_\infty + \Delta t C_1 (\gamma_1 + \gamma_2) \leq \|\nabla c(\cdot, 0)\|_\infty \\ &\quad + TC_1 (\gamma_1 + \gamma_2) \leq C_2 + TC_1 (\gamma_1 + \gamma_2). \end{aligned}$$

It should be observed that the above estimate holds for any explicit SSP ODE solver, which consists of a convex combination of forward Euler time-steps.

Parabolic-Elliptic Case ($\tau = 0$). In this case, taking a discrete gradient of (3.4) results in a linear algebraic system for $\{\nabla c_{\ell,m}\}$, which can be written using (3.5) as follows:

$$\begin{aligned} -v \left[\frac{\nabla c_{\ell+1,m} - 2\nabla c_{\ell,m} + \nabla c_{\ell-1,m}}{(\Delta x)^2} + \frac{\nabla c_{\ell,m+1} - 2\nabla c_{\ell,m} + \nabla c_{\ell,m-1}}{(\Delta y)^2} \right] + \zeta \nabla c_{\ell,m} \quad (\text{B.2}) \\ = \gamma_1 (\nabla \rho_1)_{\ell,m} + \gamma_2 (\nabla \rho_2)_{\ell,m}. \end{aligned}$$

It is well-known that the block tri-diagonal matrix on the left-hand side of (B.2) is symmetric, positive definite, and the L^∞ -norm of its inverse is uniformly bounded, say, by a constant C_3 . This immediately implies the following bound:

$$\|\nabla c\|_\infty \leq C_3 C_1 (\gamma_1 + \gamma_2),$$

which completes the proof of the theorem. \square

Funding The work of A. Chertock was supported in part by NSF grant DMS-2208438. The work of S. Cui was supported in part by Shenzhen Science and Technology Program (JCYJ20240813095709013), Guangdong Basic and Applied Basic Research Foundation (2024A1515012329), and NSFC grant 12471382. The work of A. Kurganov was supported in part by NSFC grants 12171226 and W2431004. The work of C. Wang was supported in part by NSFC grant 12401524 and China Postdoctoral Science Foundation (No. 2024M761273).

Data Availability The data that support the findings of this study and FORTRAN codes developed by the authors and used to obtain all of the presented numerical results are available from the corresponding author upon reasonable request.

Declarations

Conflicts of Interest On behalf of all authors, the corresponding author states that there is no conflict of interest.

References

1. Acosta-Soba, D., Guillén-González, F., Rodríguez-Galván, J. R.: An unconditionally energy stable and positive upwind DG scheme for the Keller-Segel model, *J. Sci. Comput.*, **97**, Paper No. 18 (2023)
2. Acosta-Soba, D., Guillén-González, F., Rodríguez-Galván, J.R.: An unconditionally energy stable and positive upwind DG scheme for the Keller-Segel model. *J. Sci. Comput.* **97**, 18–27 (2023)
3. Badia, S., Bonilla, J., Gutiérrez-Santacreu, J.V.: Bound-preserving finite element approximations of the Keller-Segel equations. *Math. Models Methods Appl. Sci.* **33**, 609–642 (2023)
4. Bergdorf, M., Cottet, G.-H., Koumoutsakos, P.: Multilevel adaptive particle methods for convection-diffusion equations. *Multiscale Model. Simul.* **4**, 328–357 (2005)
5. Bouchut, F., James, F.: Duality solutions for pressureless gases, monotone scalar conservation laws, and uniqueness. *Comm. Partial Differential Equations* **24**, 2173–2189 (1999)
6. Chertock, A.: A practical guide to deterministic particle methods, in *Handbook of numerical methods for hyperbolic problems*, vol. 18 of *Handb. Numer. Anal.*, Elsevier/North-Holland, Amsterdam, 177–202 (2017)
7. Chertock, A., Cui, S., Kurganov, A.: Hybrid finite-volume-particle method for dusty gas flows. *SMAI J. Comput. Math.* **3**, 139–180 (2017)
8. Chertock, A., Doering, C.R., Kashdan, E., Kurganov, A.: A fast explicit operator splitting method for passive scalar advection. *J. Sci. Comput.* **45**, 200–214 (2010)
9. Chertock, A., Du Toit, P., Marsden, J.E.: Integration of the EPDiff equation by particle methods. *ESAIM Math. Model. Numer. Anal.* **46**, 515–534 (2012)
10. Chertock, A., Epshteyn, Y., Hu, H., Kurganov, A.: High-order positivity-preserving hybrid finite-volume-finite-difference methods for chemotaxis systems. *Adv. Comput. Math.* **44**, 327–350 (2018)
11. Chertock, A., Kurganov, A.: On a practical implementation of particle methods. *Appl. Numer. Math.* **56**, 1418–1431 (2006)
12. Chertock, A., Kurganov, A.: A second-order positivity preserving central-upwind scheme for chemotaxis and haptotaxis models. *Numer. Math.* **111**, 169–205 (2008)
13. Chertock, A., Kurganov, A., Liu, Y.: Finite-volume-particle methods for the two-component Camassa-Holm system, *Commun. Comput. Phys.* **27**, 480–502 (2020)
14. Chertock, A., Kurganov, A., Lukáčová-Medviďová, M., Özcan, C.N.: An asymptotic preserving scheme for kinetic chemotaxis models in two space dimensions. *Kinet. Relat. Models* **12**, 195–216 (2019)
15. Chertock, A., Kurganov, A., Ricchiuto, M., Wu, T.: Adaptive moving mesh upwind scheme for the two-species chemotaxis model. *Comput. Math. Appl.* **77**, 3172–3185 (2019)
16. Chertock, A., Kurganov, A., Rykov, Y.: A new sticky particle method for pressureless gas dynamics. *SIAM J. Numer. Anal.* **45**, 2408–2441 (2007)
17. Chertock, A., Levy, D.: Particle methods for dispersive equations. *J. Comput. Phys.* **171**, 708–730 (2001)
18. Chertock, A., Liu, J.-G., Pendleton, T.: Elastic collisions among peakon solutions for the Camassa-Holm equation. *Appl. Numer. Math.* **93**, 30–46 (2015)
19. Chorin, A.J.: Numerical study of slightly viscous flow. *J. Fluid Mech.* **57**, 785–796 (1973)
20. Conca, C., Espejo, E., Vilches, K.: Remarks on the blowup and global existence for a two species chemotactic Keller-Segel system in \mathbb{R}^2 . *European J. Appl. Math.* **22**, 553–580 (2011)
21. Cottet, G.-H., Koumoutsakos, P.D.: *Vortex methods*. Cambridge University Press, Cambridge, Theory and practice (2000)
22. Cui, S., Kurganov, A., Medovikov, A.: Particle methods for PDEs arising in financial modeling. *Appl. Numer. Math.* **93**, 123–139 (2015)
23. Degond, P., Mas-Gallic, S.: The weighted particle method for convection-diffusion equations. I. The case of an isotropic viscosity. *Math. Comp.* **53**, 485–507 (1989)
24. Degond, P., Mustieles, F.-J.: A deterministic approximation of diffusion equations using particles. *SIAM J. Sci. Statist. Comput.* **11**, 293–310 (1990)
25. Eldredge, J.D., Leonard, A., Colonius, T.: A general deterministic treatment of derivatives in particle methods. *J. Comput. Phys.* **180**, 686–709 (2002)
26. Espejo, E., Vilches, K., Conca, C.: Sharp condition for blow-up and global existence in a two species chemotactic Keller-Segel system in \mathbb{R}^2 . *European J. Appl. Math.* **24**, 297–313 (2013)
27. Espejo, E.E., Stevens, A., Suzuki, T.: Simultaneous blowup and mass separation during collapse in an interacting system of chemotactic species. *Differential Integral Equations* **25**, 251–288 (2012)
28. Gottlieb, S., Ketcheson, D., Shu, C.-W.: *Strong stability preserving Runge-Kutta and multistep time discretizations*, World Scientific Publishing Co. Pte. Ltd., Hackensack, NJ (2011)
29. Gottlieb, S., Shu, C.-W., Tadmor, E.: Strong stability-preserving high-order time discretization methods. *SIAM Rev.* **43**, 89–112 (2001)

30. Griebel, M., Schweitzer, M. A.: A particle-partition of unity method for the solution of elliptic, parabolic, and hyperbolic PDEs. *SIAM J. Sci. Comput.*, 22, pp. 853–890 (electronic) (2000)
31. Gutiérrez-Santacreu, J.V., Rodríguez-Galván, J.R.: Analysis of a fully discrete approximation for the classical Keller-Segel model: Lower and a priori bounds. *Comput. Math. Appl.* **85**, 69–81 (2021)
32. Herrero, M.A., Velázquez, J.: Chemotactic collapse for the Keller-Segel model. *J. Math. Biol.* **35**, 177–194 (1996)
33. Herrero, M.A., Velázquez, J.: A blow-up mechanism for a chemotaxis model. *Ann. Scuola Norm. Sup. Pisa Cl. Sci. (4)* **24**, 633–683 (1997)
34. Hillen, T., Painter, K.J.: A user’s guide to PDE models for chemotaxis. *J. Math. Biol.* **58**, 183–217 (2009)
35. Keller, E.F., Segel, L.A.: Initiation of slime mold aggregation viewed as an instability. *J. Theoret. Biol.* **26**, 399–415 (1970)
36. Keller, E.F., Segel, L.A.: Model for chemotaxis. *J. Theor. Biol.* **30**, 225–234 (1971)
37. Kurganov, A., Lukáčová-Medvidová, M.: Numerical study of two-species chemotaxis models. *Discrete Contin. Dyn. Syst. Ser. B* **19**, 131–152 (2014)
38. Mas-Gallic, S., Poupaud, F.: Approximation of the transport equation by a weighted particle method. *Transport Theory and Stat. Phys.* **17**, 311–345 (1988)
39. Othmer, H.G., Stevens, A.: Aggregation, blowup, and collapse: the ABCs of taxis in reinforced random walks. *SIAM J. Appl. Math.* **57**, 1044–1081 (1997)
40. Patlak, C.S.: Random walk with persistence and external bias. *Bull. Math. Biophys.* **15**, 311–338 (1953)
41. Peskin, C.S.: The immersed boundary method. *Acta Numer* **11**, 479–517 (2002)
42. Puckett, E.G.: Vortex methods: an introduction and survey of selected research topics, in *Incompressible computational fluid dynamics: trends and advances*, pp. 335–407. Cambridge Univ. Press, Cambridge (2008)
43. Raviart, P.-A.: An analysis of particle methods, in *Numerical methods in fluid dynamics* (Como, vol. 1127 of Lecture Notes in Math. Springer, Berlin **1985**, 243–324 (1983)
44. Senba, T., Suzuki, T.: Parabolic system of chemotaxis: blowup in a finite and the infinite time, *Methods Appl. Anal.*, 8 (2001), pp. 349–367. *IMS Workshop on Reaction-Diffusion Systems* (Shatin, 1999)
45. Shen, J., Xu, J.: Unconditionally bound preserving and energy dissipative schemes for a class of Keller-Segel equations. *SIAM J. Numer. Anal.* **58**, 1674–1695 (2020)
46. Wolansky, G.: Multi-components chemotactic system in the absence of conflicts. *European J. Appl. Math.* **13**, 641–661 (2002)

Publisher’s Note Springer Nature remains neutral with regard to jurisdictional claims in published maps and institutional affiliations.

Springer Nature or its licensor (e.g. a society or other partner) holds exclusive rights to this article under a publishing agreement with the author(s) or other rightsholder(s); author self-archiving of the accepted manuscript version of this article is solely governed by the terms of such publishing agreement and applicable law.